Full length article

Nonlinear two-dimensional transient thermoelastic analysis of functionally graded composite plates subjected to localised cooling loads

Alireza Babaee [a,*], Jasmin Jelovica [a,b,*]

[a] *Department of Mechanical Engineering, The University of British Columbia, Vancouver, BC, Canada*
[b] *Department of Civil Engineering, The University of British Columbia, Vancouver, BC, Canada*

ARTICLE INFO

ABSTRACT

In this study, for the first time, localized thermal cooling is considered for the transient thermoelastic response of an axisymmetric plate, addressing the underexplored area of localized low-temperature thermoelasticity. Functionally graded composite plates are analyzed which consist of a mixture of stainless steel (*SUS*304) and low-carbon steel (*AISI*1020). A two-dimensional transient heat conduction equation is employed to capture localized cooling effects, featuring various adaptive time-dependent thermal boundary conditions which mirror both loading and unloading scenarios, effectively simulating real-world phenomena. Novel parameters are introduced to facilitate a comprehensive understanding of various aspects of thermal load handling and their impact on thermoelastic responses. The heat conduction equations are solved using the Generalized Differential Quadrature Method (GDQM) and the Crank-Nicolson scheme. The nonlinear governing equations, incorporating geometrical nonlinearity through the von Kármán assumption within the First Shear Deformation Theory (FSDT) framework, are solved using the GDQM and the Picard's technique. The model is validated using Finite Element Method (FEM) through Abaqus. A comprehensive analysis is provided that considers influence of the ratio of thermally affected and unaffected plate surface, thermal load magnitude, rapidity of thermal loading and unloading, duration of the cooling load, geometrical nonlinearity, and temperature dependence of material. The study shows that the maximum von Mises stress within the structure remains consistent regardless of the duration of the cooling load, as long as the rate at which the cooling load is applied stays the same. Additionally, the findings reveal that even minor localized thermal loads can produce substantial stress, especially at the intersection of thermally affected and non-affected zones on the exposed surface in some situations.

1. Introduction

1.1. Background

Engineering structures across various industries experience a diverse range of thermal loads. In case of sudden temperature drop, significant thermal stresses can arise, posing risks to structural integrity. Situations like this can arise in cryogenic fluid storage structures, medical imaging devices or other engineering structures. Analyzing structural response under low-temperature loads, particularly those involving localized loads in scenarios like cryogenic spills, is crucial for design, safety, and reliability. Better understanding the response in such situations can lead to more resilient structures withstanding diverse thermal conditions.

1.2. Literature survey

To start, it should be mentioned that many research studies offered valuable insights into the effects of elevated-temperature partial thermal loads on structural components, investigating bending, buckling, vibrations, and similar problems. Some notable contributions include Cheung et al.'s analytical solution for transient thermal stress in a hollow sphere under partial thermal loadings [1], Sugano's analytical solution for a nonhomogeneous hollow circular plate subjected to unaxisymmetric partial heating [2], and Ishihara and coauthors' investigation of transient thermoelastoplastic bending in a circular plate subjected to heat supply [3]. Ootao and Tanigawa studied three-dimensional transient thermal stress problem in a functionally graded material (FGM) rectangular plate with simple support under partial heat supply [4]. Their results show quantitative comparisons of

---

stress components in the transient state, contributing to the understanding of FGM under thermal loading. Zhuang and Swansson studied localized thermal buckling in louver-type combustor liners using nonlinear finite element method (FEM) [5]. Their findings highlight the detrimental effects of thermal loading, including buckling, increased cyclic inelastic strain, and reduced material strength and life expectancy due to local overheating. Morimoto et al. analyzed the thermal buckling of functionally graded (FG) rectangular plates under partial heating, considering uniform temperature rise through their thickness [6]. Analytical methods were developed to determine in-plane resultant forces and calculate critical buckling temperatures using the Galerkin method. The results show that material inhomogeneity, aspect ratio, and heated region significantly influence the critical buckling temperatures. Ohmichi and Noda presented an analytical solution for plane thermal stresses in graded plates subjected to partial heating [7]. Numerical calculations were performed for two cases, revealing the distribution of maximum stresses and temperatures. The results demonstrate that suitable selection of compositional materials can significantly reduce thermal stresses in the plates. Ootao and Tanigawa investigated the theoretical of transient thermoelastic problems in orthotropic FGM rectangular plates with nonuniform partial heat supply [8]. The study presents an exact three-dimensional solution for the transient temperature, displacement, and stress distributions. The influence of material nonhomogeneity and orthotropy is also examined, providing precise evaluations of transverse shear stresses and normal stress in the thickness direction during the transient state. Fallah and Noseir analyzed FG circular plates subjected to asymmetric loading and heat conduction, highlighting the limitations of linear theory [9]. Gaikwad explored thermoelastic deformation of a thin hollow circular disk under partially distributed and axisymmetric heat supply [10]. Jabbari et al. studied the thermoelastic behavior of various FG structures. They analyzed non-symmetric steady-state thermal stresses in graded hollow cylinders using power series [11], and developed an analytical solution for stress in FGM short hollow cylinders using Bessel functions [12]. They also examined a three-dimensional FGM circular plate under partial axisymmetric load [13], highlighting variations between FG plates and isotropic materials. Ootao and Ishihara analyzed transient thermoelastic problems in a multilayered hollow FGM cylinder due to asymmetrical partial heating [14]. Their numerical calculations demonstrated the influence of FGM medium on thermal stresses and the effectiveness of the multilayered FGM model in reducing maximum stresses. Kumar et al. conducted studies on the stability of composite structures [15,16]. They investigated the stability of cylindrical panels under mechanical and localized thermal loadings and developed analytical expressions for pre-buckling stresses. They also studied the thermal buckling behavior of rectangular plates subjected to localized heating, considering thermoelasticity and nonlinear stability. Their research highlighted the influence of load type, imperfections, aspect ratio, and material properties on the stability of the composite structure. Bhagat and Jeyaraj experimentally assessed the buckling strength of a non-uniformly, locally heated cylindrical panel, considering the influence of temperature field type, boundary conditions, and panel aspect ratio [17]. Their results revealed the significant impact of the temperature field on the buckling strength, with the least stiff region exposed to the highest temperature exhibiting reduced buckling strength. Nguyen Van Do et al. studied the thermal buckling behavior of FGM plates under full and partially heating loads using isogeometric analysis and a refined higher-order shear deformation theory [18]. Their numerical method accurately predicted the buckling responses and emphasized the significance of considering 3-D heat conduction effects. Ehrhardt and Virgin explored the buckling behavior of thin clamped panels under elevated partial thermal loading [19]. They investigated factors like symmetry, boundary conditions, and geometric imperfections that influence post-buckling shapes. Amiri Delouei et al. provided a steady-state analytical solution for two-dimension heat conduction in FGM cylindrical sectors [20]. They presented an illustrative example which reveals distinct temperature

distribution patterns resulting from material non-homogeneity. Ren et al. studied the thermo-mechanical buckling behavior of a non-uniformly locally heated rectangular plate with temperature-dependent material properties [21]. The study reveals the influence of surrounding temperature fields, in-plane load cases, and aspect ratio on the thermo-mechanical behavior of the plate.

In the field of civil engineering, Refs. [22–25] have collectively enhanced understanding of localized fire thermal loads, by investigating the thermal responses of non-uniformly heated structures, the feasibility of dimensionally reduced heat transfer analysis, and the buckling behavior and fire resistance of structures under such conditions. While there is a considerable amount of research on structural responses at elevated temperatures, response of structures at low-temperatures has been studied far less. Even within this area, the focus is usually directed to fracture mechanics in cryogenic environments, however, thermoelastic analysis is crucial for fundamental understanding of the response. Even localized low-temperature thermal loads can induce significant thermal stress, as shown in this study, potentially causing severe structural damage.

Various studies have analyzed fractures at low temperatures, predominantly examining cryogenic crack propagation. For example, a study by Sandia National Laboratory researchers examined potential thermal damage from cryogenic incidents in liquified natural gas (LNG) cargo vessels. Using advanced computational models, they discovered that embrittlement in the hull section was a major cause of fracture [26]. In a study by Kalan and Petti, a series of tests were conducted to examine crack propagation in steel plates exposed to cryogenic spills [27]. Their experimental design comprised four distinct phases to investigate several parameters, including temperature profile, cooling rate, material properties, and fracture characteristics. Baalisampang et al. proposed a numerical approach to investigate the effects of small to medium-sized LNG spills on steel structures [28]. They integrated ANSYS FEM structural module with a CFD tool to conduct transient thermal and structural analyses. Their process began with a static analysis on crack-free geometry to identify areas of maximum von Mises stress, followed by a fracture analysis on a cracked geometry. In another relevant study, De Beer and colleagues conducted a thorough investigation on the effects of cryogenic spills on floating LNG tankers, with a focus on quantifying the risk of fractures due to cryogenic thermal shock [29]. Their work emphasizes the necessity of understanding crack formation, predicting crack progression, and identifying the spill sizes that could compromise the structure's integrity. A study by Oh and his team utilized the Abaqus FEM software to investigate the influence of insulation layers on cryogenic-induced thermal shock in composite laminates [30]. The study concluded that an insulation layer significantly reduced the maximum stress, mitigating the risk of delamination and matrix cracking. There are also various other studies that consider the safety and risk assessment of cryogenic liquid containers, covering topics from bunkering technologies to post-accident analyses [31–34].

1.3. Present study

According to the literature survey, the field of low-temperature thermoelasticity, particularly under partial (localized) loading conditions, remains an unexplored area of research. Addressing this research gap, the current study extends the prior work done by the same authors on transient thermoelastic response of plates [35]. Current study conducts a nonlinear transient thermoelastic analysis on axisymmetric plates, subjected to localized cooling. The methodology introduces novel unique parameters, aiming for a more in-depth understanding of deflections and stresses that develop. The axisymmetric plate utilized in this study is made of graded material composition, with stainless steel (*SUS*304) on the exposed side and low-carbon steel (*AISI*1020) on the opposite side. The material properties are temperature-dependent, based on experimental data. To capture localized cooling effects, two-dimensional transient heat conduction equations with novel
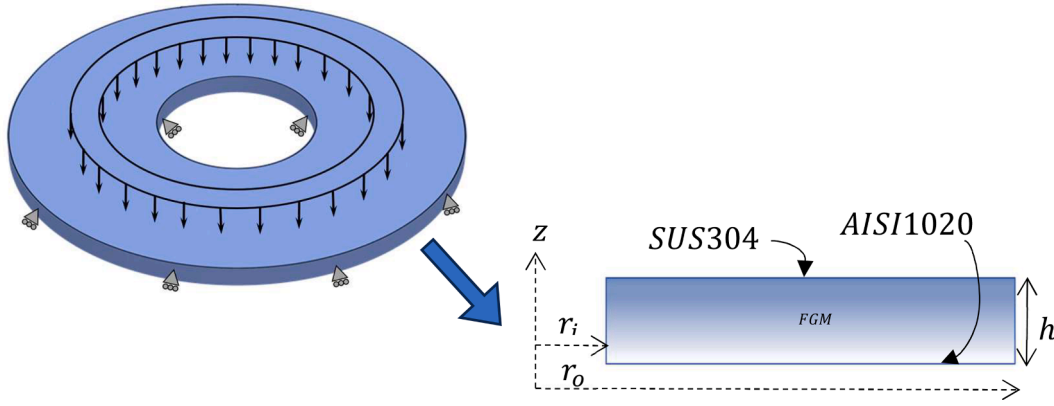
Fig. 1. Illustration of an annular/circular plate exposed to arbitrary partial transverse thermal load.

varying time-dependent boundary conditions are utilized, solved through the Generalized Differential Quadrature Method (GDQM) and the Crank-Nicolson scheme. First-order Shear Deformation Theory (FSDT) framework is used to represent the plate. Given the potential for significant deflections, geometrical nonlinearity through the von Kármán assumption is considered. This leads to the derivation of a set of nonlinear governing equations using Hamilton's principle, and solutions are subsequently obtained through the GDQM and Picard's technique. The model is validated using finite element software Abaqus.

2. Theoretical formulation and methodology

2.1. Geometry and effective material properties of media

We consider a circular/annular plate with the following dimensions: inner radius (r_i), outer radius (r_o), and thickness (h). This plate experiences an axisymmetric rapid thermal load. Fig. 1 illustrates the plate. We adopt a cylindrical coordinate system (r, θ, z) with the origin situated at the plate's mid-plane center. Within this coordinate system, r, θ, and z correspond to the radial, circumferential, and thickness directions, respectively. Notably, if r_i equals zero, the annular plate transforms into a solid circular plate.

FGMs have demonstrated effective performance under challenging thermal conditions, such as rapid cooling or heat shock loads [36]. This study uses stainless steel (*SUS*304) and carbon steel (*AISI*1020) to create the graded material. Fig. 1 illustrates the arrangement, where *SUS*304 is positioned on the side exposed to low temperature thermal load due to its stable properties at such temperatures. Conversely, *AISI*1020 is located on the opposite side, to benefit from its superior weldability and lower cost. To achieve functionally graded medium along the thickness direction, the power law model is employed. The volume fractions V_i and V_j correspond to *SUS*304 and *AISI*1020, respectively, while ξ represents the power law model index.

$$V_i = \left(0.5 + \frac{z}{h}\right)^{\xi}, \; V_j = 1 - V_i \tag{1}$$

The thermomechanical properties, including density (ρ), specific heat capacity (C_v), coefficient of thermal expansion (α), thermal conductivity (κ), Young's modulus (E), and Poisson's ratio (ν), are determined through the application of the Voigt model [36].

$$P(z, T) = P_j(T) + P_{ij}(T)V_i$$
$$P_{ij}(T) = P_i(T) - P_j(T) \tag{2}$$

As indicated in Eq. (2), P_i and P_j represent the thermomechanical properties of each constituent material. In previous studies conducted by the same authors (Refs. [35,37]), the impact of temperature dependency on the thermoelastic behavior at low temperatures has been demonstrated. Consequently, the current study incorporates

temperature-dependent data obtained from Tables 1 and 2 in Refs. [35, 37]. These tables provide curve-fitted material properties for *SUS*304 and *AISI*1020 based on experimental data specifically collected at low temperatures.

2.2. Displacement field

Due to the axisymmetric geometry, loading, and boundary conditions of the plate, the thermoelastic response is expected to exhibit axisymmetric behavior. The First-order Shear Deformation Theory (FSDT) is employed to analyze the plate's behavior. In the polar coordinate system, the radial displacement (u) and transverse displacement (w) of an arbitrary point on the plate are described by the following equation.

$$u(r, z, t) = u_0(r, t) + z\varphi_r(r, t)$$
$$w(r, t, z) = w_0(r, t) \tag{3}$$

In the provided equations, the variables w_0 and u_0 represent the midplane transverse and radial displacements, respectively. Additionally, φ_r represents the rotation of the normal about the θ axis.

2.3. Nonlinear strain-displacement relations

Considering the significant influence of geometrical nonlinearity on the elastic response of the plate, as demonstrated by authors [35], it is crucial to incorporate this effect. By utilizing the von Kármán assumption, the nonlinear strain-displacement relations can be expressed as follows:

$$\varepsilon_{rr} = u_{,r} + \frac{1}{2}w_{,r}^2$$
$$\varepsilon_{\theta\theta} = \frac{1}{r}u \tag{4}$$
$$\gamma_{rz} = u_{,z} + w_{,r}$$

$\varepsilon_{\theta\theta}$ and ε_{rr} represent the hoop and radial strains, respectively, while γ_{rz} denotes the shear strain. Substituting Eq. (3) into Eq. (4) yields the following expression:

$$\varepsilon_{rr} = u_{0,r} + z\varphi_{r,r} + \frac{1}{2}w_{0,r}^2$$
$$\varepsilon_{\theta\theta} = \frac{1}{r}(u_0 + z\varphi_r) \tag{5}$$
$$\gamma_{rz} = \varphi_r + w_{0,r}$$

2.4. Constitutive equations

For a thermoelastic axisymmetric plate under thermal loading, the constitutive relation can be described according to Ref. [38]. Eq. (6)

introduces the stiffness coefficients (Q_{ij}) expressed in terms of engineering constants.

$$\begin{Bmatrix} \sigma_{rr} \\ \sigma_{\theta\theta} \\ \tau_{rz} \end{Bmatrix} = \begin{bmatrix} Q_{11} & Q_{12} & 0 \\ Q_{12} & Q_{22} & 0 \\ 0 & 0 & Q_{55} \end{bmatrix} \left(\begin{Bmatrix} \varepsilon_{rr} \\ \varepsilon_{\theta\theta} \\ \gamma_{rz} \end{Bmatrix} - (\Delta T) \begin{Bmatrix} \alpha \\ \alpha \\ 0 \end{Bmatrix} \right) \tag{6}$$

$$Q_{11} = Q_{22} = \frac{E(z,T)}{1 - \nu^2(z,T)}, \quad Q_{12} = \frac{\nu(z,T)E(z,T)}{1 - \nu^2(z,T)}, \quad Q_{55} = \frac{E(z,T)}{2(1 - \nu(z,T))} \tag{7}$$

2.5. Stress resultants

As per the FSDT, the force and moment resultants can be expressed as described in Ref. [37].

$$(N_{rr}, \ N_{\theta\theta}, \ M_{rr}, \ M_{\theta\theta}, \ Q_{rz}) = \int_{-\frac{h}{2}}^{\frac{h}{2}} (\sigma_{rr}, \ \sigma_{\theta\theta}, \ z\sigma_{rr}, \ z\sigma_{\theta\theta}, K_s\tau_{rz})dz \tag{8}$$

Using the transverse shear strain correction factor K_s (assumed to be 5/6 [39]), the force and moment resultants can be expressed according to Ref. [38]. Substituting Eqs. (5) and (6) into Eq. (8) provides the stress resultants in terms of displacements.

$$\begin{Bmatrix} N_{rr} \\ N_{\theta\theta} \\ M_{rr} \\ M_{\theta\theta} \\ Q_{rz} \end{Bmatrix} = \begin{bmatrix} A_{11} & A_{12} & B_{11} & B_{12} & 0 \\ A_{12} & A_{22} & B_{12} & B_{22} & 0 \\ B_{11} & B_{12} & D_{11} & D_{12} & 0 \\ B_{12} & B_{22} & D_{12} & D_{22} & 0 \\ 0 & 0 & 0 & 0 & K_s A_{55} \end{bmatrix} \begin{Bmatrix} u_{0,r} + \frac{1}{2}w_{0,r}^2 \\ \frac{1}{r}u_0 \\ \varphi_{r,r} \\ \frac{1}{r}\varphi_r \\ w_{0,r} + \varphi_r \end{Bmatrix} - \begin{Bmatrix} N^T \\ N^T \\ M^T \\ M^T \\ 0 \end{Bmatrix} \tag{9}$$

$$(A_{ij}, \ B_{ij}, \ D_{ij}) = \int_{-\frac{h}{2}}^{\frac{h}{2}} Q_{ij} \left(1, \ z, z^2\right) dz \tag{10}$$

$$(N^T, \ M^T) = \int_{-\frac{h}{2}}^{\frac{h}{2}} \frac{E(z,T)\alpha(z,T)}{1 - \nu(z,T)} \left(T(r,\theta, \ z) - T_0(r,\theta, \ z)\right)(1, \ z)dz \tag{11}$$

2.6. Equations of motion

By employing Hamilton's principle, the governing equations can be derived [38]. In the current study, the virtual kinetic energy (δT) and virtual external work (δV) are assumed to be zero. Hence, the virtual strain energy (δU) of the plate is defined as follows.

$$\int_{t_1}^{t_2} \delta\Pi \, dt = \int_{t_1}^{t_2} (\delta\mathcal{T} - (\delta U + \delta V))dt = 0$$

$$\delta U = \int_{r_i}^{r_o} \int_{-\frac{h}{2}}^{\frac{h}{2}} \left(\sigma_{rr}\delta\varepsilon_{rr} + \sigma_{\theta\theta}\delta\varepsilon_{\theta\theta} + K_s\tau_{rz}\delta\gamma_{rz} \right) \, rdzdr \tag{12}$$

The governing equations for the axisymmetric plate under localized thermal load are derived by substituting Eqs. (5), (6), and (8) into Eq. (12), integrating across the z and r directions, and conducting subsequent mathematical manipulations.

$$\delta u_0 \rightarrow N_{rr,r} + \frac{1}{r}(N_{rr} - N_{\theta\theta}) = 0$$

$$\delta w_0 \rightarrow \frac{1}{r}(rN_{rr}w_{0,r})_{,r} + Q_{rz,r} + \frac{1}{r}Q_{rz} = 0 \tag{13}$$

$$\delta\varphi_r \rightarrow M_{rr,r} + \frac{1}{r}(M_{rr} - M_{\theta\theta}) - Q_{rz} = 0$$

As the thermal load is localized, it should be noted that the derivatives of A_{ij}, B_{ij}, D_{ij}, N^T, and M^T with respect to r appear in the following equations.

$$\delta u_0 \rightarrow A_{11}\left(u_{0,rr} + \frac{1}{r}u_{0,r} - \frac{1}{r^2}u_0 + w_{0,r}w_{0,rr} + \frac{1}{2r}w_{0,r}^2\right) - \frac{A_{12}}{2r}w_{0,r}^2$$
$$+ B_{11}\left(\varphi_{r,rr} + \frac{1}{r}\varphi_{r,r} - \frac{1}{r^2}\varphi_r\right) + A_{11,r}\left(u_{0,r} + \frac{1}{2}w_{0,r}^2\right) + A_{12,r}\left(\frac{u_0}{r}\right)$$
$$+ B_{11,r}(\varphi_{r,r}) + B_{12,r}\left(\frac{1}{r}\varphi_r\right) - N_{,r}^T$$
$$= 0$$

$$\delta w_0 \rightarrow A_{55}\left(\varphi_{r,r} + \frac{1}{r}\varphi_r + w_{0,rr} + \frac{1}{r}w_{0,r}\right) + K_sA_{55,r}\left(w_{0,r} + \varphi_r\right)$$
$$+ A_{11}\left(\frac{1}{r}u_{0,r}w_{0,r} + \frac{1}{2r}w_{0,r}^3 + w_{0,rr}u_{0,r} + \frac{3}{2}w_{0,rr}w_{0,r}^2 + w_{0,r}u_{0,rr}\right)$$
$$+ \frac{A_{12}}{r}\left(w_{0,rr}u_0 + w_{0,r}u_{0,r}\right) + B_{11}\left(\frac{1}{r}w_{0,r}\varphi_{r,r} + w_{0,rr}\varphi_{r,r} + w_{0,r}\varphi_{r,rr}\right)$$
$$+ B_{12}\left(\frac{1}{r^2}w_{0,r}\varphi_r + \frac{1}{r}w_{0,r}\varphi_{r,r}\right) + A_{11,\ r}\left(u_{0,r}w_{0,r} + \frac{1}{2}w_{0,r}^3\right)$$
$$+ A_{12,\ r}\left(\frac{1}{r}u_0w_{0,r}\right) + B_{11,r}(\varphi_{r,r}w_{0,r}) + B_{12,r}\left(\frac{1}{r}\varphi_rw_{0,r}\right)$$
$$- N^T\left(w_{0,rr} + \frac{1}{r}w_{0,r}\right) - N_{,r}^T(w_{0,r})$$
$$= 0$$

$$\delta\varphi_r \rightarrow B_{11}\left(u_{0,rr} + \frac{1}{r}u_{0,r} - \frac{1}{r^2}u_0 + w_{0,r}w_{0,rr} + \frac{1}{2r}w_{0,r}^2\right) - \frac{B_{12}}{2r}w_{0,r}^2$$
$$+ D_{11}\left(\varphi_{r,rr} + \frac{1}{r}\varphi_{r,r} - \frac{1}{r^2}\varphi_r\right) - A_{55}\left(w_{0,r} + \varphi_r\right) + B_{11,r}\left(u_{0,r} + \frac{1}{2}w_{0,r}^2\right)$$
$$+ B_{12,r}\left(\frac{u}{r}\right) + D_{11,r}(\varphi_{r,r}) + D_{12,r}\left(\frac{\varphi_r}{r}\right) - M_{,r}^T$$
$$= 0$$
$$\tag{14}$$

The boundary conditions are determined in the following manner.

$$\delta u_0 = 0 \ or \ N_{rr} = 0$$
$$\delta\varphi_r = 0 \ or \ M_{rr} = 0 \tag{15}$$
$$\delta w_0 = 0 \ or \ Q_{rz} + N_{rr}w_{0,r} = 0$$

The immovable and movable simply supported boundary conditions at the edges of the plate can be expressed as:

- *Immovable Simply supported* (*IMSS*) :
  $u_0 = w_0 = M_{rr} = 0$

  Movable Simply supported (*MSS*) :
  $N_{rr} = w_0 = M_{rr} = 0$ \hfill (16)

Throughout this study, the *IMSS* boundary condition is consistently applied unless specified otherwise. For a solid circular plate (without a hole), the following boundary condition should be satisfied.

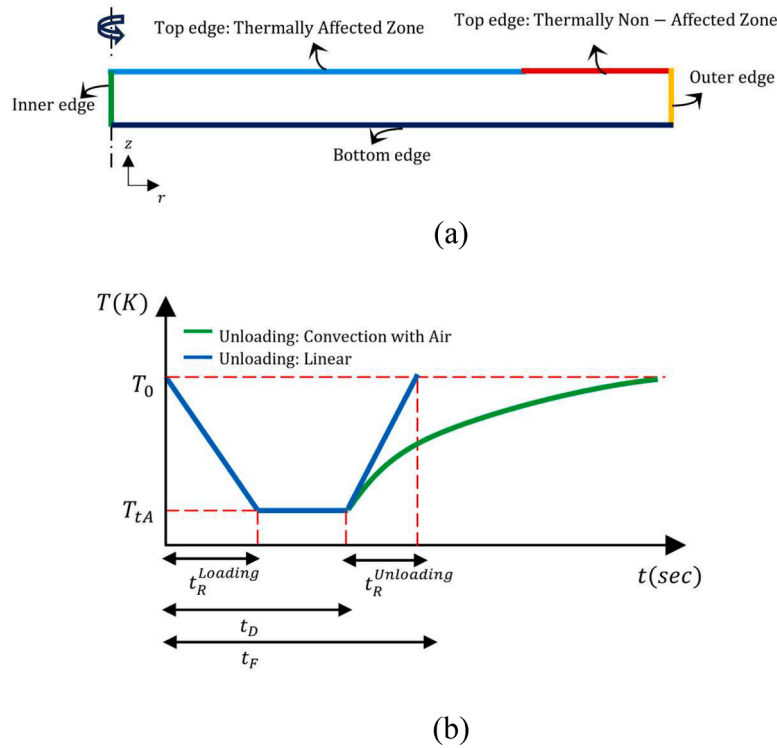$$@r_i = 0: \ u_0 = \varphi_r = Q_{rz} + N_{rr}w_{0,r} = 0 \tag{17}$$

Fig. 2. (a) Illustration of thermal boundary conditions on different edges of the plate; (b) time-variant loading and unloading phases on the thermally affected zone of the plate's top surface.

2.7. Solution methodology

Obtaining analytical solutions can be challenging due to the strong geometrical and material nonlinearities present in the governing equations as outlined in Eq. (14). In this context, we utilize a renowned approach known as the Generalized Differential Quadrature Method (GDQM) to unravel the governing equations. As demonstrated in the literature, GDQM is a highly effective and computationally-friendly numerical approach [40–44]. An extended discussion about the GDQM is available in the Appendix.

Applying the GDQM to Eqs. (14) through (17) transforms them into their following matrix format.

$$[K(T, \mathscr{X})] \{\mathscr{X}\} = \{\mathscr{F}(T)\} \tag{17}$$

In this new form, $[K(T, \mathscr{X})]$ is defined as the stiffness matrix that is dependent on temperature and displacement, $\{\mathscr{X}\}$ is displacement vector and $\{\mathscr{F}(T)\}$ is the temperature dependent force vector. Eq. (17), which consists of a group of nonlinear algebraic equations, can be solved using a method known as Direct Picard's iterative algorithm, as explained in Ref. [45].

$$\{\mathscr{X}\}_{s+1} = \left[K(T, \{\mathscr{X}\}_s)\right]^{-1} \{\mathscr{F}(T)\}$$
$$\text{Convergence criterion :} \sqrt{\left(\{\mathscr{X}\}_{s+1} - \{\mathscr{X}\}_s\right)^2 / \left(\{\mathscr{X}\}_{s+1}\right)^2} < \varepsilon \tag{18}$$

Starting at $s = 1$, the procedure in Eq. (18) continues until the difference between two sequential $\mathscr{X}$ approximations becomes smaller than the preset value (ε).

2.8. Heat transfer equation

The transient heat conduction equation provides the two-dimensional temperature variation in cylindrical coordinates for an axisymmetric plate under arbitrary partial thermal load, over space and time.

$$\frac{1}{r} \frac{\partial}{\partial r} \left(r.\kappa(z, T) \frac{\partial T(r, \theta, z)}{\partial r} \right) + \frac{1}{r^2} \frac{\partial}{\partial \theta} \left(\kappa(z, T) \frac{\partial T(r, \theta, z)}{\partial \theta} \right)$$
$$+ \frac{\partial}{\partial z} \left(\kappa(z, T) \frac{\partial T(r, \theta, z)}{\partial z} \right) + \dot{e}_{gen} = \rho(z, T) C_v(z, T) \dot{T} \tag{19}$$

Assuming the partial thermal load to be axisymmetric and disregarding the heat generation term, Eq. (19) can be expressed in two dimensions:

$$\frac{1}{r} \kappa(z, T) \frac{\partial T(r, \theta, z)}{\partial r} + \frac{\partial \kappa(z, T)}{\partial r} \frac{\partial T(r, \theta, z)}{\partial r} + \kappa(z, T) \frac{\partial^2 T(r, \theta, z)}{\partial r^2}$$
$$+ \frac{\partial \kappa(z, T)}{\partial z} \frac{\partial T(r, \theta, z)}{\partial z} + \kappa(z, T) \frac{\partial^2 T(r, \theta, z)}{\partial z^2} = \rho(z, T) C_v(z, T) \dot{T} \tag{20}$$

As indicated by Eq. (20), to capture the localized thermal load effect, the temperature changes in both r and z directions. Consequently, as shown in Fig. 2(a), various boundary conditions are applied to five specific edges: the top edge within and outside of the thermally affected zone, the inner edge, the bottom edge, and the outer edge.

Within the thermally affected zone on the top edge, the loading phase is approached via two distinct methods: 1) prescribed temperature input and 2) prescribed heat flux input. For each approach, adaptive, time-dependent boundary conditions on the thermally affected top edge are defined. These conditions, characterized by unique parameters $t_R^{Loading}$, $t_R^{Unloading}$, t_D and t_F, are detailed in Fig. 2(b). These parameters define different aspects of thermal load handling: $t_R^{Loading}$ represents the time period during which the thermal load is applied (loading phase), $t_R^{Unloading}$ signifies the time period during which the thermal load decreases (unloading phase), t_D indicates the duration of the thermal load in loading phase and t_F is the total final time including both loading and unloading phases.

The motivation behind assuming an unloading phase, particularly one involving convection with air (as shown in Fig. 2(b)), lies in enhancing the accuracy of the model to better replicate the physical

phenomenon under investigation. This becomes particularly significant when a low-temperature or cryogenic liquid spill occurs on the top surface, which, after a specific duration (t_D), boils off and evaporates. The unloading phase is thus crucial for capturing this aspect of the phenomenon. The mathematical expression for the time varying prescribed temperature and heat flux boundary conditions on top edge within the thermal affected zone are provided in Eq. (21).

For the five edges shown in Fig. 2(a), various boundary conditions including prescribed temperature, heat flux, insulation, and air convection are considered. The inner edge always assumes insulation to ensure axisymmetric scenarios involving a solid circular geometry. The corresponding mathematical expressions for these conditions are provided in Eqs. (21) and (22).

the GDQM, and time derivatives in Eq. (23) are approximated using the Crank-Nicolson method [45].

$$[C_T(T)]\{\dot{T}\} + [K_T(T)]\{T\} = \{F_T(T)\} \tag{23}$$

An iterative procedure is necessary due to material nonlinearity. The steps are summarized below.

1. Apply the Crank-Nicolson scheme ($\alpha = 0.5$) to fully discretize Eq. (23) at t_{s+1}, yielding

$$\{T\}_{s+1} = [\widehat{K_T}(T)]^{-1}_{s+1}\{\widehat{F_T}(T)\}_{s,\,s+1}$$

$$[\widehat{K_T}(T)]_{s+1} = [C_T(T)] + a_1[K_T(T)]_{s+1}$$

$$\mathcal{T}(r,z,t) = \begin{cases} Loading\ phase: \ \left(\dfrac{T_{tA} - T_0}{t_R^{Loading}}\right)t + T_0, t < \ t_R^{Loading}\ (sec) \\[4mm] Loading\ phase: \ T_t, t_R^{Loading} \le t \le t_D\ (sec) \\[4mm] Unloading\ phase\ (linear): \ \left(\dfrac{T_0 - T_{tA}}{t_R^{Unloading}}\right)(t - t_D) + T_0, t_D < t \le \ t_F\ (sec) \\[4mm] (r,\ z) \in \ Top\ Edge\ Thermally\ Affected\ Zone \end{cases}$$

$$\mathcal{q}''(r,z,t) = \begin{cases} Loading\ phase: \ \left(\dfrac{q_t''}{t_R^{Loading}}\right)t, t < \ t_R^{Loading}\ (sec) \\[4mm] Loading\ phase: \ q_t'', t_R^{Loading} \le t \le t_D\ (sec) \\[4mm] Unloading\ phase\ (linear): \ \left(\dfrac{-q_t''}{t_R^{Unloading}}\right)(t - t_D) + q_t'', t_D < t \le \ t_F\ (sec) \\[4mm] (r,\ z) \in \ Top\ Edge\ Thermally\ Affected\ Zone \end{cases} \tag{21}$$

$$\{\widehat{F_T}(T)\}_{s,\,s+1} = \left([C_T(T)] - a_2[K_T(T)]_s\right)\{T\}_s + a_1\{F_T(T)\}_{s+1} + a_2\{F_T(T)\}_s$$

$$a_1 = \alpha\Delta t,\ a_2 = (1 - \alpha)\Delta t \tag{24}$$

2. Evaluate properties at $T = T_0$ and compute $\{T\}_{s+1}$ using the Eq. (24) from step 1.
3. Refresh properties with the temperature from step 2, and re-calculate $\{T\}_{s+1}$.
4. Iterate step 3 until temperature converges.
5. Proceed to next time increment ($s \to s+1$), repeat steps 2–5 until solution is obtained.

3. Results and discussions

This section presents the implementation of our proposed technique to investigate the transient thermoelastic response of an axisymmetric plate subjected to a localized low-temperature thermal load. The solid circular plate's inner radius is specified numerically as $r_i = 10^{-8}\ m$. W_{mid} stands for the maximum mid-plane transverse displacement in circular and annular plates at defined radii. Computations for radial, hoop, and von Mises stresses are performed on the upper face ($z = +h/2$) and given radius, unless specified otherwise. The boundary condition is immovable simple support (IMSS) throughout, except if mentioned otherwise. The analysis employs $t_R^{Loading} = 0.01\ sec$, and the temperatures ($T_{tN}, T_b, T_o, T_0, T_\infty$) are maintained at 293 K, with the

Top edge: thermally affected zone:

- Prescribed temperature:
- Prescribed heat flux:
- Convection with air:

Bottom edge:

- Prescribed temperature:
- Thermally insulated:
- Convection with air:

Inner edge:

Thermally insulated: $\dfrac{\partial T(r,z)}{\partial r} = 0$ due to the axisymmetric assumption for solid circular plate

Top edge: thermally non-affected zone: (22)

- Prescribed temperature:
- Thermally insulated:
- Convection with air:

Outer edge:

- Prescribed temperature:
- Thermally insulated:
- Convection with air:

Initial condition:

$T(r,z,t) = T_0$

In Eqs. (21) and (22), $\mathcal{T}(r,z,t)$ and $q''(r,z,t)$ denote the time-varying temperature and heat flux at the affected top edge, respectively, while, T_{tA} and q_t'' indicate the preset temperature and heat flux at the same location, respectively. $T_{tN}, T_b, T_o, T_0, T_\infty$ and $\hbar$ represent the temperature at the non-affected top edge, bottom edge, outer edge, initial temperature, ambient air temperature, and convective heat transfer coefficient, respectively.

Given that temperature significantly impacts thermal properties (κ and C_v), and can follow a complex pattern, finding an analytical solution for Eq. (20) is challenging. Therefore, the heat equation is discretized via
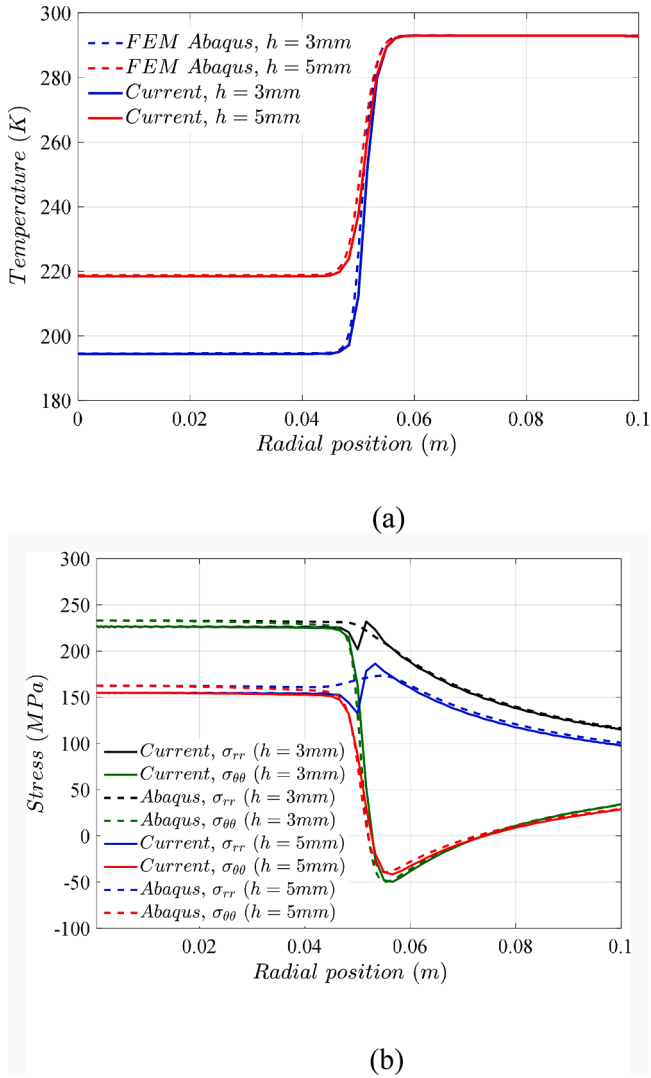
(a)

(b)

Fig. 3. Validation of (a) temperature, (b) radial and hoop stress on the mid-plane ($z = 0$) of the solid circular plate subjected to localized low-temperature thermal load at $t = 1$ sec.

thermally affected zone temperature T_{tA} set at 93 K. The convection heat transfer $\hbar$ is presumed to be 25 $Wm^{-2}K^{-1}$. As underscored by the authors' previous research [35], thermoelastic response accuracy is contingent upon the temperature dependency of material properties. Consequently, the results are based on temperature-dependent material properties, with the validation section as an exception where temperature-independent properties are employed. In this study, the Partial Load Ratio (*PLR*) is introduced as a key parameter to quantify the proportion of the top face of the plate that is subjected to the localized thermal load. The *PLR* is calculated by the ratio of the radius of the thermally affected zone to the outer radius of the plate, i.e., *PLR* = $r_{thermally\ affected\ zone}/r_o$. The thermal load is applied on the top face (surface), adjacent to the inner edge.

3.1. Validation and comparison studies

As stated above, available literature does not provide any similar studies on the thermoelastic response under localized low-temperature thermal loading. Therefore, a comparative analysis was conducted to validate the proposed formulation and its results by comparing them with those obtained from finite element software Abaqus (ver. 6.22).

Two case studies were examined, involving circular plates with thickness of $h = 3mm$ and $h = 5mm$. The plates were composed of stainless steel (*SUS*304) and had a radius of $r_o = 100mm$, with *IMSS* boundary conditions. A rapid cooling load of $T_{tA} = 93\ K$, with *PLR* of 50 %, was applied to the thermally affected top surface. The outer edge was set to *'prescribed temperature'*, the non-affected top edge was subjected to *'convection with air'*, and the bottom and inner/outer edges were assigned as *'prescribed temperature'* and *'insulated'*, respectively. These results were obtained for a total time of $t_F = 1$ sec.

Fig. 3(a) and (b) depict a comparison of temperature, radial and hoop stresses versus radial position for the circular plate using the current methodology and Abaqus. The FEM model utilized an axisymmetric plate geometry with CAX4T solid elements and a coupled temperature-displacement solver that considered geometrical nonlinearity. The mesh consisted of 100 elements in the thickness direction and 800 elements in the radial direction. Results demonstrate a high level of agreement between the temperatures, radial stresses (σ_{rr}), and hoop stresses ($\sigma_{\theta\theta}$) computed using the current approach and Abaqus. This agreement indicates high accuracy of the current methodology. The figure shows that the hoop stress changes from tensile in the thermally affected zone to compressive in the nearby part of the non-affected zone. This is because the tensile thermal component predominates in the affected zone, whereas in the non-affected zone, the absence of a thermal gradient means the mechanical component governs the hoop stress.

3.2. Parametric studies

3.2.1. Effect of partial load ratio (PLR)

Fig. 4 illustrates the influence of the Partial Load Ratio (*PLR*) on the temperature distribution across the spatial domain (vertical and radial directions) of a circular plate. The plate has an outer radius of $r_o = 100mm$ and a thickness of $h = 5mm$, and it is subjected to a rapid cooling thermal load of $T_{tA} = 93\ K$. The *PLR* varies from 20 % up to 100 %, representing both localized and full load cases, and is applied to the thermally affected top surface. For the localized thermal loading cases, the outer, bottom, and non-affected top edges were set to *'prescribed temperature'*, while the inner edges were assigned as *'insulated'*. These results were obtained for a time duration of $t_F = 3$ sec. Observing Fig. 4 (a)–(c), it can be noted that when the *PLR* is less than 100 %, heat is conducted in two directions (radial and vertical). However, in the case of full load (*PLR* = 100%), heat conduction occurs solely in the vertical direction.

Fig. 5 depicts the influence of the *PLR* on deflection (W_{mid}) and von Mises stress (σ_{VM}) over time, as well as the von Mises stress across the radial position at $t = 1$ sec. The circular plate, with an outer radius (r_o) of 100mm and thickness (h) of 3mm, is subjected to a rapid cooling thermal load of $T_{tA} = 93\ K$, with varying *PLR* values. The outer and bottom edges have a *'prescribed temperature'*, the thermally non-affected top edge experiences *'convection with air'*, while the inner edge remains *'insulated'*.

Fig. 5(a) shows the temperature distribution at the top of the plate where various *PLR* values are plotted. As seen in Fig. 5(b), increasing the *PLR* percentage leads to a proportional rise in the maximum deflection (W_{mid}) over time. This effect arises from the increased thermal load on the plate's top surface, resulting in greater deflection. As time progresses and the temperature stabilizes within the structure, the deflection decreases and reaches a steady state.

In Fig. 5(c), the general trend showcases a gradual decrease in σ_{VM} values, moving from the plate's center towards the outer edge, except at the intersection of the affected and thermally non-affected zones. This sharp increase in σ_{VM} at the intersection is attributed to the relatively higher temperature difference in that region, caused by the thermal boundary condition on the top edge, leading to increased thermal stress. Interestingly, the maximum σ_{VM} does not necessarily occur at the circular plate's center (r_i) for all *PLR* values. For smaller *PLR* values, the maximum σ_{VM} occurs at the intersection of affected and non-affected
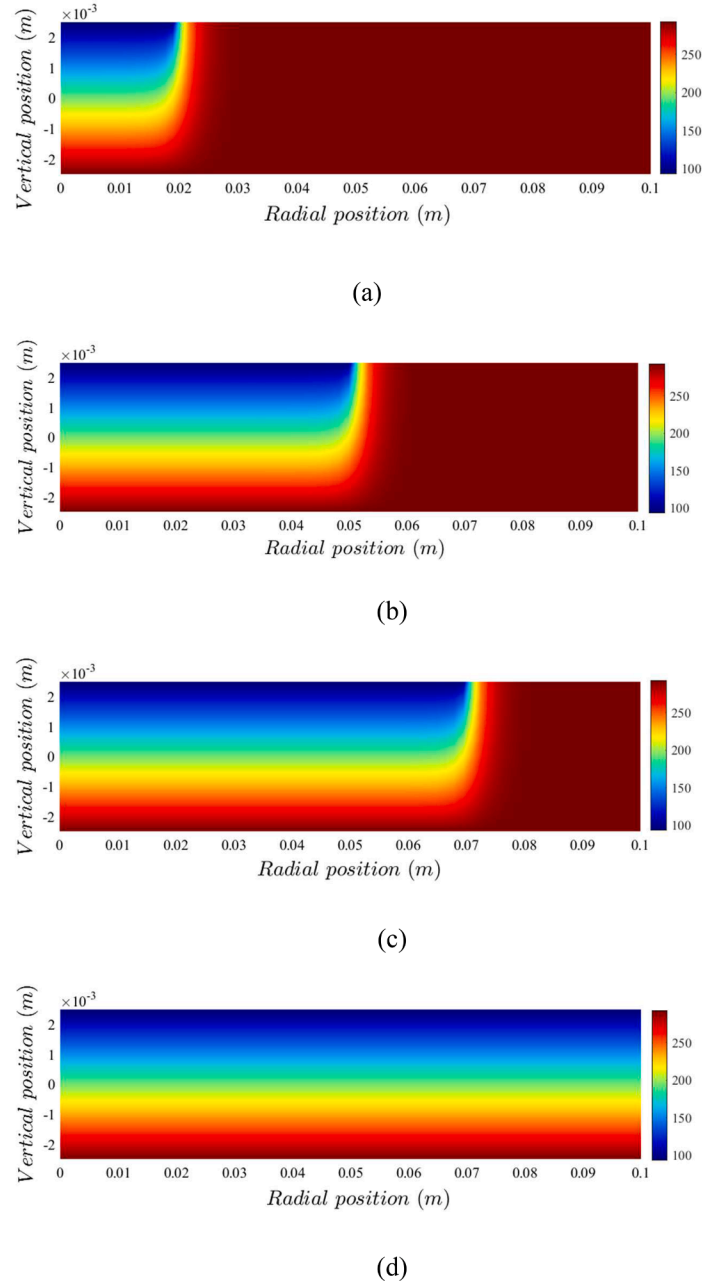
(a)

(b)

(c)

(d)

Fig. 4. Temperature contour in the spatial domain after 3 *sec* for circular plate under low-temeprature thermal load with different *PLRs*: (a) *PLR* = 20%, (b) *PLR* = 50%, (c) *PLR* = 70%, and (d) *PLR* = 100%.

thermal zones. This observation highlights the significance of properly analyzing localized thermal loads. In Fig. 5(d), σ_{VM} against time is presented with different *PLR* values, with σ_{VM} calculated at $r = r_i$. As evident, applying the thermal load results in a rapid increase in σ_{VM}, which gradually decreases over time, reaching a steady state at $t = 1$ *sec*. It can be seen that the stress is large even for a small *PRL* values.

3.2.2. Effect of thermal loading rapidity time ($t_R^{Loading}$)

The thermal loading rapidity time $t_R^{Loading}$ represents how fast is the thermal load applied on the plate's top face (see Fig. 2(b) for graphical visualization). Fig. 6 illustrates the influence of $t_R^{Loading}$ on temperature change and W_{mid} over time, σ_{VM} across the radial position, and σ_{VM} over time. The circular plate has an outer radius (r_o) of 100*mm*, thickness (h)

of 5*mm*, and $\xi = 0.5$, subjected to a rapid cooling thermal load ($T_{tA} = 93\ K$) with *PLR* of 50 %. The inner, outer, and bottom edges are *'insulated'*, while the thermally non-affected top edge has *'convection with air'* boundary conditions. Results were obtained for $t_F = 15$ *sec*.

Fig. 6(a) presents the temperature at the top face within the thermally loaded zone plotted against time. Increasing $t_R^{Loading}$ from 0.01 *sec* to 10 *sec* means that the temperature decreases from 293K (T_0) to 93K (T_{tA}) within those specified time values. Smaller values of $t_R^{Loading}$ correspond to a faster thermal load application, leading to a more abrupt thermal shock, while larger values mean the load is applied at a slower pace. In Fig. 6(b), W_{mid} vs. time is displayed for various $t_R^{Loading}$ values. It is evident that increasing $t_R^{Loading}$ significantly affects W_{mid}, with the maximum magnitude of W_{mid} decreasing. Additionally, the time at
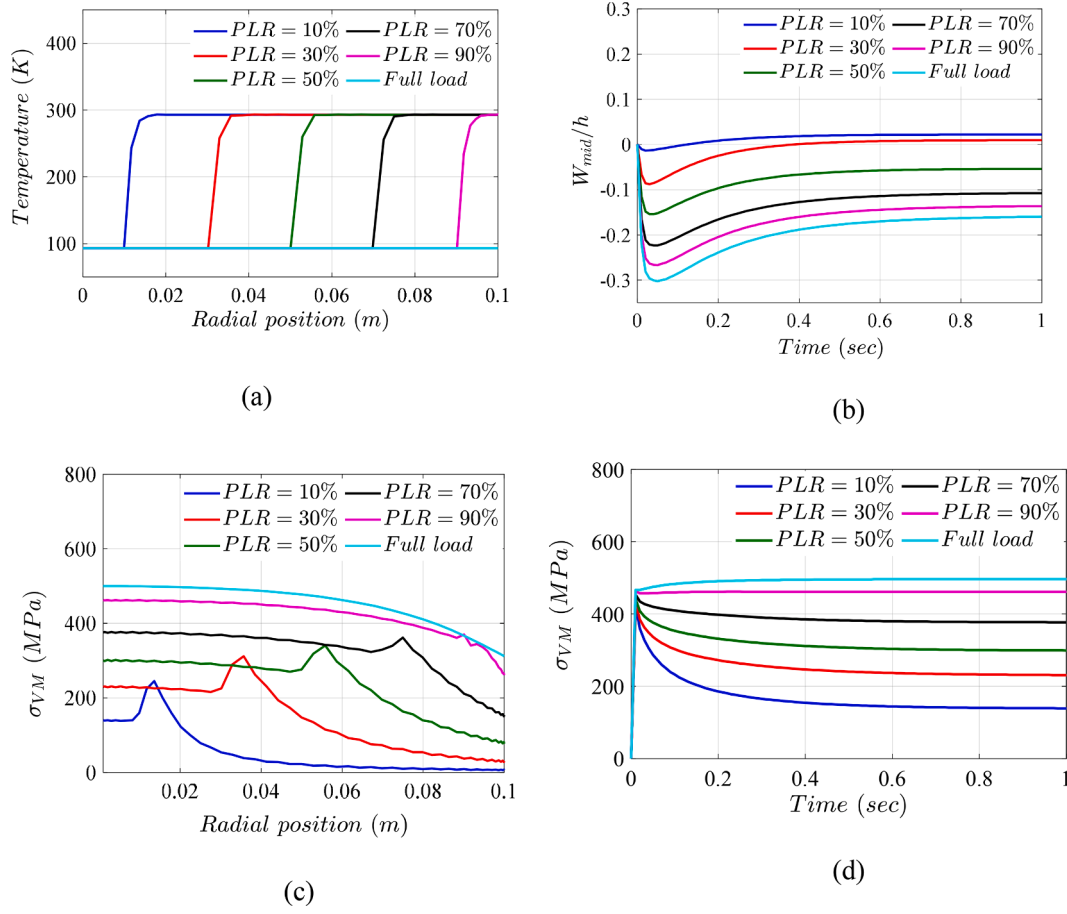
Fig. 5. The effect of *PLR* on: (a) temperature over radial position at the top face and at $t = 1 \; sec$, (b) lateral deflection (W_{mid}) over time, (c) von Mises stress (σ_{VM}) at the top face across the radial position at $t = 1 \; sec$, and (d) von Mises stress (σ_{VM}) over time at the top face and $r = r_i$.

which the maximum deflection magnitude occurs shifts with increasing $t_R^{Loading}$.

Fig. 6(c) shows σ_{VM} against radial position at $t = 15 \; sec$ for different $t_R^{Loading}$ values. The trend indicates that σ_{VM} decreases by moving from the center of the plate (r_i) towards the outer edge (r_o), except at the intersection between the thermally affected and non-affected zones, where there is a sharp increase in σ_{VM}. Increasing $t_R^{Loading}$ leads to a decrease in σ_{VM} across all radial positions. Furthermore, a small relative increase in $t_R^{Loading}$ from 5 s to 10 s (two times) results in a greater decrease in σ_{VM} compared to a larger relative increase in $t_R^{Loading}$ (e.g., from 0.01 s to 0.5 s, which is 50 times). Therefore, the change in σ_{VM} with respect to $t_R^{Loading}$ is not linear. In Fig. 6(d), σ_{VM} is plotted against time with various $t_R^{Loading}$ values, with σ_{VM} calculated at the top face and inner edge ($r = r_i$). An interesting pattern emerges in the behavior of the von Mises stress during the loading process. At the start of the process ($t = 0$), the stress begins to increase. It continues to rise until it reaches its peak value, and the time it takes to reach this maximum is correlated with the value of the thermal loading rapidity time. This observation reveals that the time at which the stress increases is directly linked to the value of $t_R^{Loading}$, meaning that the thermal loading rapidity time has a direct impact on the maximum von Mises stress magnitude and how quickly the stress levels change. Subsequently, σ_{VM} starts to decrease and reaches a steady

state. Fig. 6 demonstrates that the rate of thermal loading is extremely important for the variation of stress and deflections in time.

3.2.3. Effect of thermal unloading rapidity time ($t_R^{Unloading}$)

The thermal unloading rapidity time ($t_R^{Unloading}$) represents how quickly the thermal load is removed from the thermally affected zone on the top face of the plate, as depicted in Fig. 2(b). This unique parameter provides valuable insights into the plate's response during the final phase. Fig. 7 shows the influence of $t_R^{Unloading}$ on the temperature, W_{mid} and σ_{VM} over time, and σ_{VM} across the radial position. The circular plate ($r_o = 100mm$, $h = 5mm$, $\xi = 0.5$) undergoes rapid cooling to $T_{tA} = 93 \; K$ with a *PLR* of 50 %. The inner, outer, and bottom edges are *'insulated'*, while the non-affected top edge experiences *'convection with air'*. Results were obtained for the total time of $t_F = 60 \; sec$, with a thermal load duration of $t_D = 30 \; sec$ on the affected zone of the top face. Two unloading approaches are considered: linear unloading and natural unloading through heat convection with air.

Fig. 7(a) illustrates the temperature change over time at the thermally loaded part of the top surface. As shown, after $t_D = 30 \; sec$, the temperature starts to increase back to the ambient temperature (unloads) within the corresponding $t_R^{Unloading}$. This indicates that with a larger $t_R^{Unloading}$, the thermal load requires more time to be removed, resulting in a longer duration of its presence on the top face.
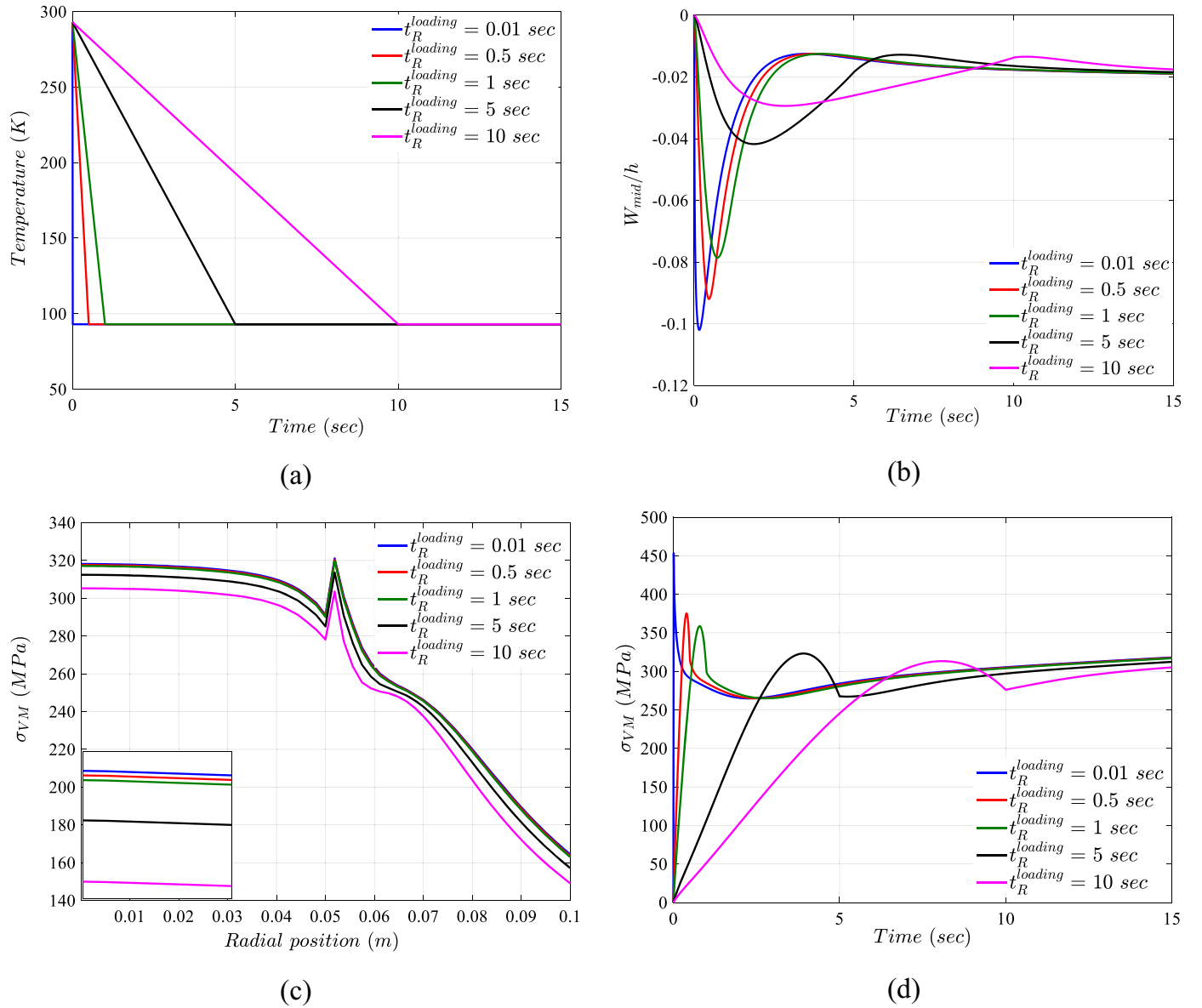
Fig. 6. The effect of thermal loading rapidity time ($t_R^{Loading}$) on: (a) temperature over time at thermally loaded zone of the top face, (b) lateral deflection (W_{mid}) over time (c) von Mises stress (σ_{VM}) across the radial position at $t = 15\ sec$ and (d) von Mises stress (σ_{VM}) over time at the top face and $r = r_i$.

Additionally, natural heat convection unloading takes the longest compared to other linear unloading cases. In Fig. 7(b), W_{mid} vs. time is plotted for various $t_R^{Unloading}$ cases. Interestingly, after the initial peak deflection during the loading phase, a second peak emerges right after the unloading phase begins. This is due to the temperature stabilization across the structure within the 30-second duration of t_D. Removing the thermal load from the top face reintroduces temperature differences, causing a change in deflections and resulting in the second peak. The timing of this second peak in the W_{mid} against time curve depends on $t_R^{Unloading}$. Smaller $t_R^{Unloading}$ values lead to a steeper peak with larger W_{mid}, while larger $t_R^{Unloading}$ values result in a less steep peak with smaller W_{mid}. In the case of unloading through heat convection, which is a gradual process, the deflection does not show a significant change.

Fig. 7(c) and (d) illustrate the relationship between σ_{VM} and radial position, and the variation of σ_{VM} over time, for different $t_R^{Unloading}$ cases. As shown in Fig. 7(d), σ_{VM} begins to increase at $t = 0$, reaching its maximum within the time defined by $t_R^{Loading}$ (loading rapidity time).

Then, after $t_D = 30\ sec$, when unloading occurs, it suddenly drops. This decline is primarily because the thermal stress, a significant contributor to σ_{VM} values, becomes negligible after thermal unloading. Furthermore, the change in σ_{VM} over time exhibits a direct correlation with the magnitude of $t_R^{Unloading}$.

3.2.4. Effect of thermal load duration time (T_D)

In this study, a unique parameter, Thermal Load Duration Time (T_D), has been introduced. It represents the duration of time for which the thermal load is maintained at a specified temperature (T_{tA}) before the unloading process begins. This consideration takes into account the evaporation effect of cryogenic liquids, for example. Fig. 8 illustrates the influence of T_D on temperature and W_{mid} over time, on σ_{VM} across the radial position at 30 sec, and on σ_{VM} over time. The circular plate ($r_o = 100mm$, $h = 5mm$, $\xi = 0.5$) is subjected to rapid cooling ($T_{tA} = 93K$) with a *PLR* of 50 %. All the edges are *'insulated'*, except for the non-loaded top edge, which experiences *'convection with air'*. During the unloading phase, the thermally affected edge also undergoes *'convection*
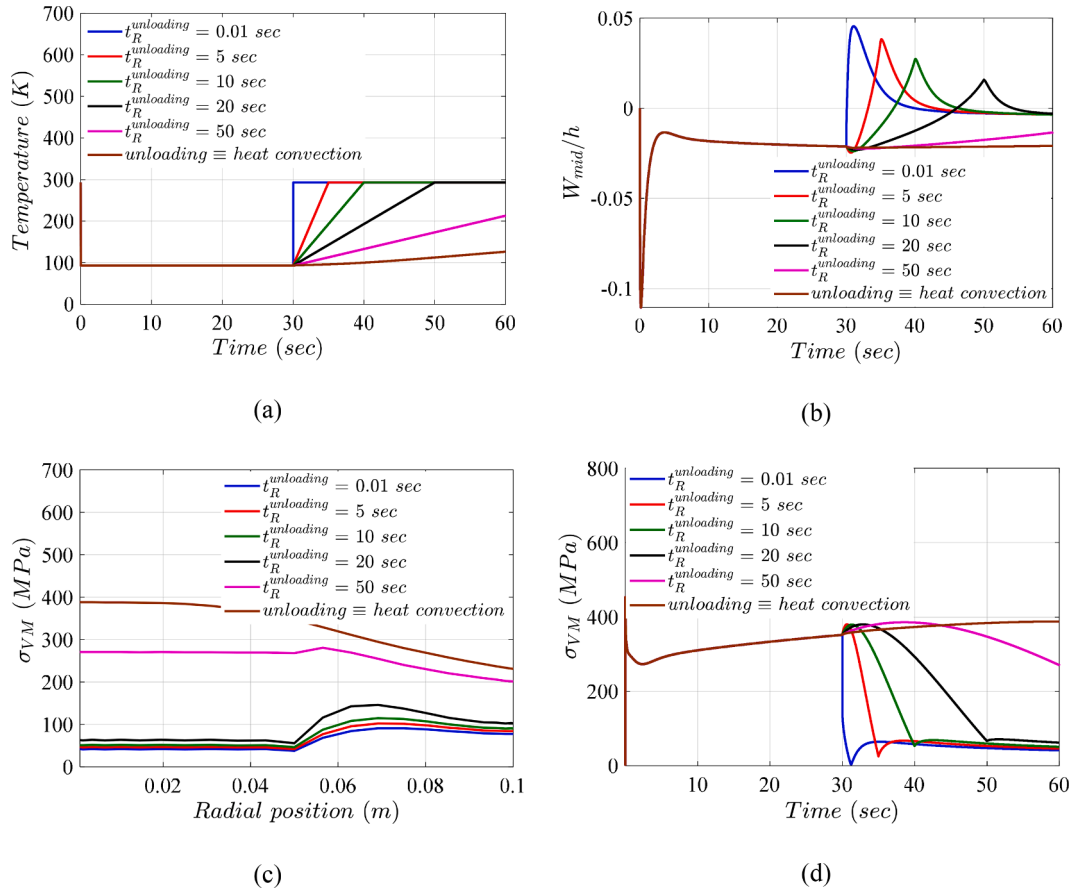
(a)

(b)

(c)

(d)

Fig. 7. The effect of thermal unloading rapidiy time ($t_R^{Unloading}$) on: (a) temperature over time at thermally loaded zone of the top face, (b) lateral deflection (W_{mid}) over time (c) von Mises stress (σ_{VM}) across the radial position at $t = 60\ sec$ and (d) von Mises stress (σ_{VM}) over time at the top face and $r = r_i$.

with air'. The results were obtained for the total time of $t_F = 30\ sec$.

Fig. 8(a) presents the temperature over time at the plate's exposed area on the top face for various T_D values. Smaller T_D values correspond to a shorter duration of the thermal load on the top face. Consequently, when the unloading occurs (after the T_D time has elapsed), the temperature rises to ambient levels more quickly compared to cases with larger T_D values. Interestingly, Fig. 8(b) reveals that the maximum W_{mid} remains identical across all cases, regardless of T_D, implying that T_D does not affect the maximum W_{mid}. However, the steady-state magnitude of W_{mid} at $t = 30\ sec$ does depend on T_D; larger T_D values result in a larger steady magnitude of W_{mid} (in absolute values).

Fig. 8(c) displays σ_{VM} on the top surface after 30 s for varying T_D values. It is evident that an increase in T_D leads to higher σ_{VM} values across the top surface. This is mainly due to the prolonged presence of the thermal load, generating additional thermal stresses. Moreover, from Fig. 8(d), we can observe that the maximum σ_{VM} occurs during the first peak, and this value remains constant regardless of T_D. This means that, no matter how long the thermal load remains at $T_{tA} = 93K$, the maximum σ_{VM} values are nearly identical. However, after the T_D time has elapsed, a second peak in the σ_{VM} occurs. It can be observed that the magnitudes of σ_{VM} in the second peak increase as the T_D value decreases. Furthermore, Fig. 8(d) indicates that the longer the thermal load remains on the top face, the larger the steady-state magnitude of σ_{VM} becomes.

3.2.5. Effect of thermal load magnitude (ΔT)

Fig. 9 depicts the impact of thermal load intensity (ΔT) on deflection and von Mises stress. Here we consider a circular plate ($r_o = 100mm$, $h = $

$3mm$, $\xi = 0$), subject to varying cooling thermal loads ($\Delta T = T_0 - T_{tA}$) and a 70 % PLR. The plate has 'insulated' inner and outer edges; the non-affected top edge undergoes 'convection with air'; the bottom edge has a 'prescribed temperature'. Results were obtained for $t_F = 1\ sec$.

Fig. 9 reveals that ΔT significantly affects both W_{mid} and σ_{VM}. Even relatively small ΔT can lead to considerable stress and deflection in the plate. As shown in Fig. 9(b), larger magnitude of ΔT increases the maximum lateral deflection (W_{mid}), and the maximum is reached sooner. Fig. 9(c) and (d) demonstrate the influence of ΔT on σ_{VM} against radial position and time, respectively. In Fig. 9(c), the distribution of von Mises stress (σ_{VM}) across the radial position of the plate is depicted. Results show that the σ_{VM} values are larger near the center of the plate compared to the outer regions. This observation is consistent with the axisymmetric condition of the plate, where deflection is more pronounced at the center (at r_i), leading to increased stress values at that location. Fig. 9 (d) depicts a sudden rise in σ_{VM} from zero to its peak within $t_R^{Loading} = 0.01\ sec$, followed by a decline until a steady state is reached. The peak σ_{VM} value significantly rises with an increase in ΔT. Notably, even a small ΔT can lead to substantial stresses, as depicted in Fig. 9(d).

3.2.6. Effect of geometrical nonlinearity

As illustrated in Fig. 10, we examined here three PRL cases (20 %, 50 %, and 80 %), each with linear and nonlinear geometric assumptions. The figure involves a circular plate ($r_o = 100mm$, $h = 3mm$, $\xi = 0$) subjected to cooling thermal loads ($T_{tA} = 93K$). The plate has 'insulated' inner edge; the thermally unaffected top edge is at 'convection with air', and the bottom and outer edges have a 'prescribed temperature'. All findings were acquired over a period of $t_F = 1\ sec$. Fig. 10(a)
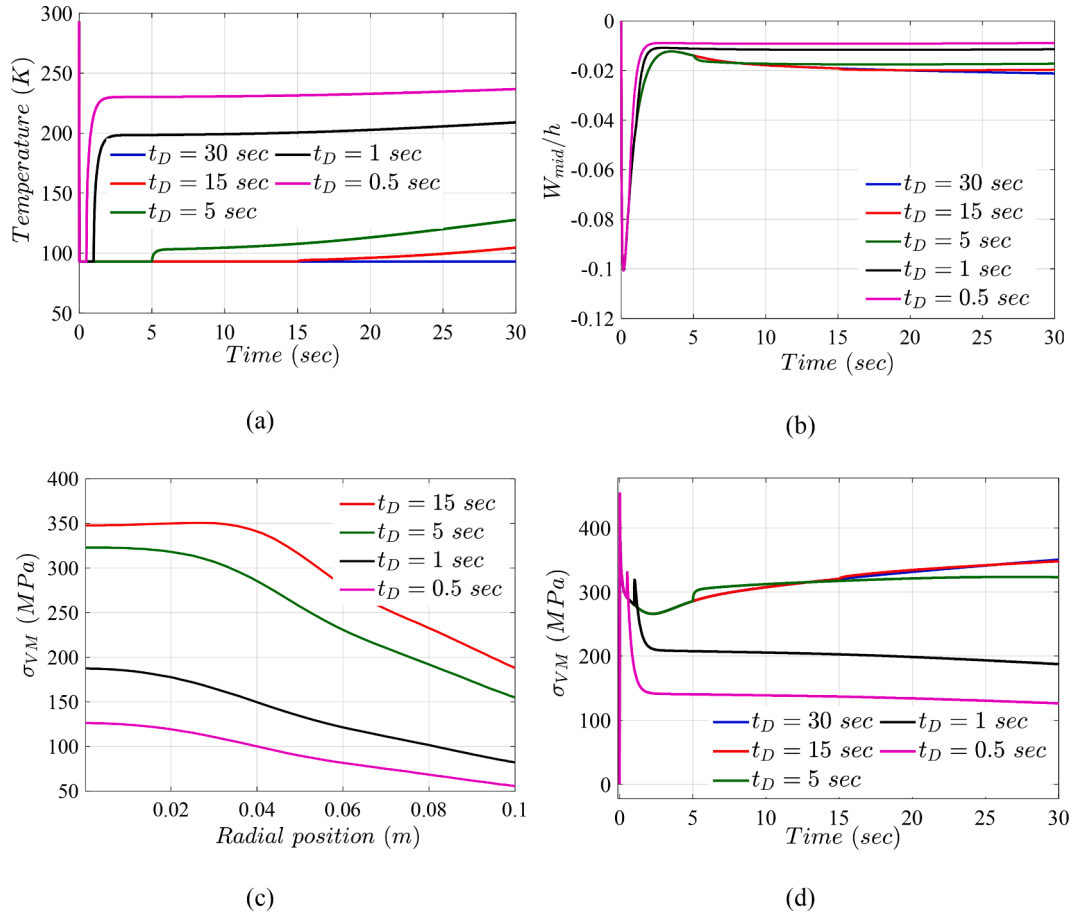
Fig. 8. The effect of thermal load duration time (t_D) on: (a) temperature over time at thermally loaded zone of the top face, (b) lateral deflection (W_{mid}) over time (c) von Mises stress (σ_{VM}) across the radial position at $t = 30\ sec$ and (d) von Mises stress (σ_{VM}) over time at the top face and $r = r_i$.

demonstrates 17.5 % discrepancy in plate deflections between the linear and nonlinear solutions when *PLR* is at 80 %. Conversely, reducing the *PLR* to 20 % (leading to more localized thermal loads) results in less than a 2 % difference between the linear and nonlinear solutions for W_{mid}. Notably, the linear assumption consistently overestimates the maximum absolute value of W_{mid}, and the steady-state W_{mid} solution may be over or underpredicted by the linear assumption, contingent on the conditions. Fig. 10(b) highlights the influence of a nonlinear geometrical assumption on σ_{VM} over time. While this assumption has less impact on σ_{VM} compared to lateral deflection, it is still recommended to uphold the geometric nonlinearity assumption for enhanced accuracy, especially for plates with larger span or lower thickness.

3.2.7. Effect of material temperature dependency

The impact of temperature-dependent (*TD*) material properties in low-temperature regime on lateral deflection of an axisymmetric plate under low-temperature thermal load has been discussed in Refs. [35, 37]. It was demonstrated that temperature-independent (*TID*) properties can result in overestimation of lateral deflections and temperature throughout the thickness. Fig. 11 presents the modulus of elasticity (*E*), thermal expansion coefficient ($\alpha_{thermal}$), thermal conductivity (κ), and specific heat capacity (C_p) plotted against thickness direction for various ΔT magnitudes. This figure is made for circular plate ($r_o = 100mm$, $h = 5mm$, $\xi = 0.5$) with 50 % *PLR*. The plate has an *'insulated'* inner edge, a *'convection with air'* top edge, and *'prescribed temperature'* for both

bottom and outer edges. Data were extracted at $t_F = 1\ sec$ and at $r = r_i$. As depicted in Fig. 11, the disparity between *TD* and *TID* is minimal with smaller ΔT magnitudes, but it becomes more pronounced with larger ΔT. Additionally, given the graded nature of the material in the thickness direction, thermomechanical properties alter across the thickness. With the assumption of *TD* properties and an increase in ΔT magnitude, the trend of these properties variation across the thickness also changes. The figure confirms that TD properties need to be considered in this type of analysis.

4. Concluding remarks

In this research, for the first time, nonlinear transient thermoelastic behavior of axisymmetric plate under localized (partial) low-temperature thermal loads is analyzed. A few newly introduced parameters including partial load ratio (*PLR*), thermal loading and unloading rapidity times ($t_R^{Loading}$) and ($t_R^{Unloading}$), thermal load duration time (T_D), thermal load magnitude (ΔT), are scrutinized for their influence on the plate deflections and stresses. In addition, influence of geometrical nonlinearity and temperature-dependent material properties is investigated.

The findings underscore the necessity of considering these factors in the design and evaluation of plates exposed to the thermal loads. The methodologies employed and the insights gained could serve as a
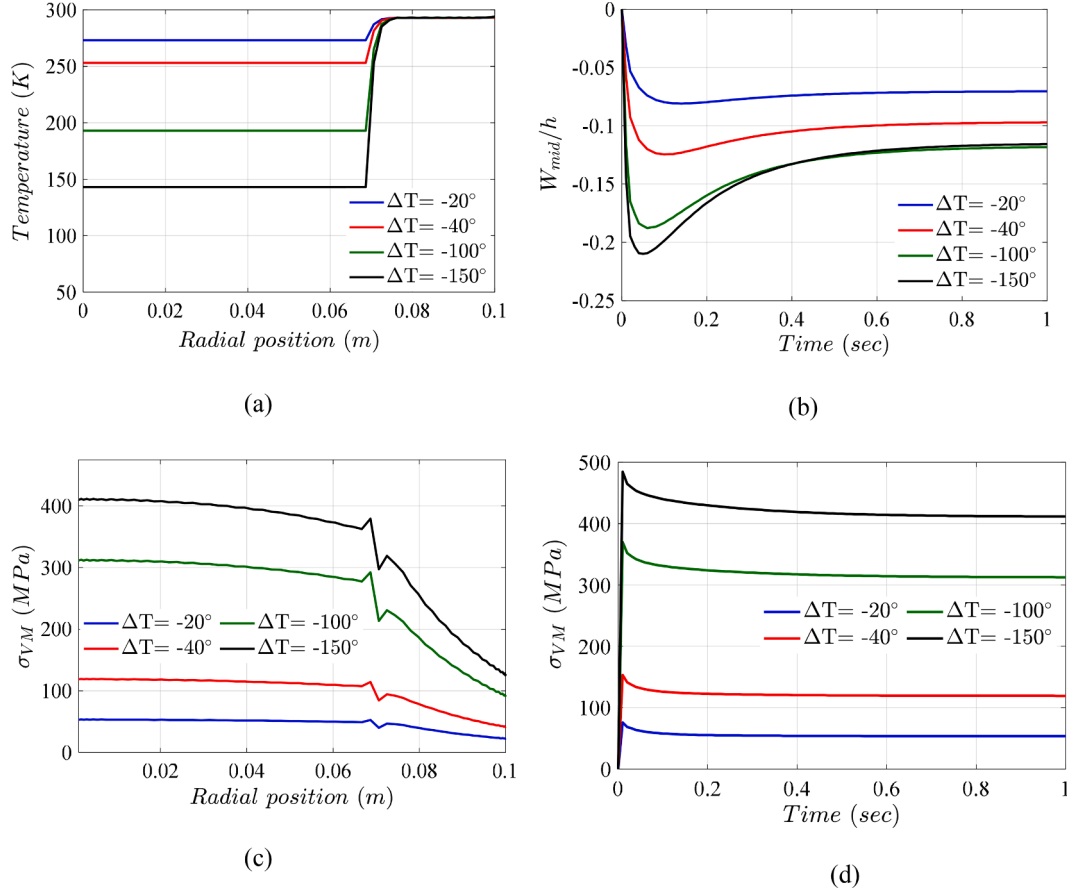
Fig. 9. The effect of thermal load magnitudes (ΔT) on: (a) temperature over radial position at the top face and at $t = 1\ sec$, (b) lateral deflection (W_{mid}) over time, (c) von Mises stress (σ_{VM}) across the radial position at $t = 1\ sec$, and (d) von Mises stress (σ_{VM}) over time at the top face and $r = r_i$.
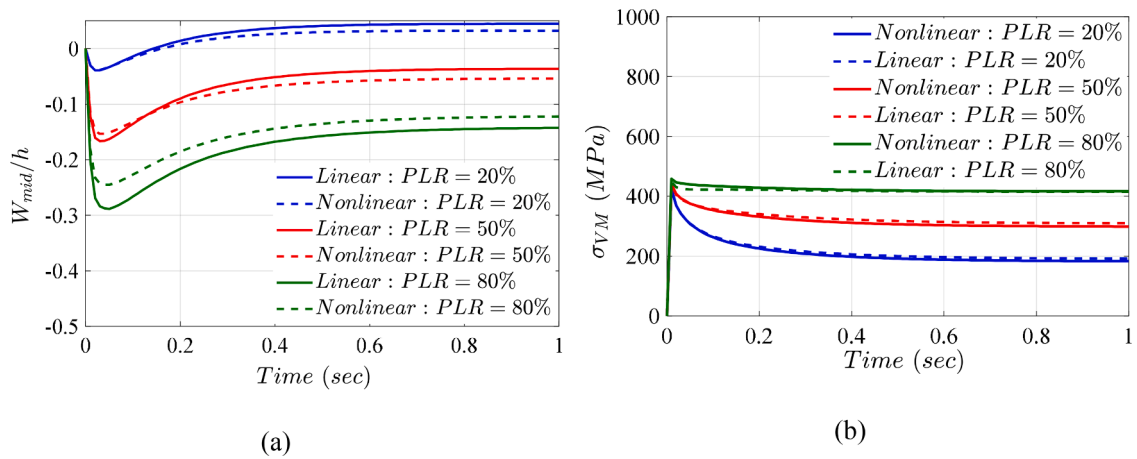

Fig. 10. The effect of geometrical nonlinearity on: (a) the lateral deflection (W_{mid}) and (b) Von Mises stress (σ_{VM}) over time.
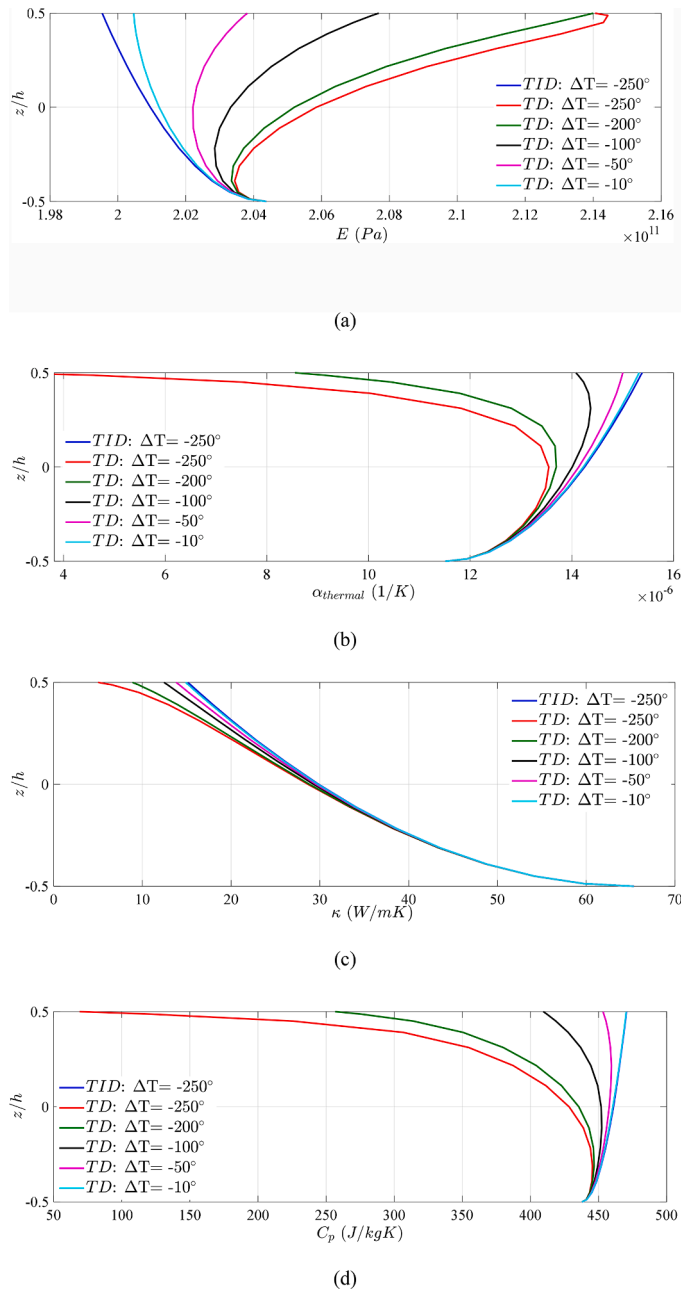
(a)

(b)

(c)

(d)

Fig. 11. The effect of FGM's material temperature dependency on (a) modulus of elasticity (E), (b) thermal expansion coefficient ($\alpha_{thermal}$), (c) thermal conductivity (κ) and (d) specific heat capacity (C_p).

resource for further studies exploring other flexural structures subjected to thermal loads. The key conclusions drawn from this study are as follows:

- Localized thermal loads can result in a significant von Mises stress at the intersection of thermally affected and non-affected zones on the exposed surface. This emphasizes the need to carefully consider localized thermal loads in structural design and analysis.
- The Partial Load Ratio (*PLR*), representing the extent of the thermal loading on the exposed surface, significantly influences the temperature distribution, deflection, and von Mises stress in a circular plate. Changes in *PLR* can lead to different response of the plate, highlighting the importance of considering localized thermal loads.
- The thermal loading rapidity time ($t_R^{Loading}$) plays a crucial role in the behavior of the plate. Variations in $t_R^{Loading}$ result in unique changes in the temperature distribution, deflection, and von Mises stress. This reveals the significance of the rate at which thermal loads are applied in assessing the performance of thermally-loaded structures.
- The thermal unloading rapidity time ($t_R^{Unloading}$) also profoundly impacts the responses of the plate. Variations in $t_R^{Unloading}$ bring about noticeable changes in temperature, deflection, and stress patterns. It underlines the importance of understanding the rate at which thermal loads are removed in evaluating thermally-loaded structures.
- The thermal load duration time (T_D) and thermal load magnitude (ΔT) parameters also hold substantial influence over the plate behavior. The maximum von Mises stress remains consistent regardless of the T_D value, as long as the $t_R^{Loading}$ stays the same. Although T_D has no impact on the maximum lateral deflection, it alters magnitude of deflection and von Mises stress in the steady-state regime.
- Factors such as geometrical nonlinearity and material temperature dependency are key for accurately predicting plate responses. Linear assumptions tend to overestimate the peak deflection, and neglecting geometrical nonlinearity can also lead to inaccuracies of the results.

CRediT authorship contribution statement

Alireza Babaee: Conceptualization, Data curation, Formal analysis, Investigation, Methodology, Software, Validation, Visualization, Writing – original draft. **Jasmin Jelovica:** Supervision, Funding acquisition, Project administration, Resources, Validation, Writing – review & editing.

Declaration of Competing Interest

The authors declare that they have no known competing financial interests or personal relationships that could have appeared to influence the work reported in this paper.

Data availability

Data will be made available on request.

Acknowledgments

Appendix

The concept of differential quadrature (DQ) postulates that the derivative of a function at a given point can be approximated by a weighted linear sum of the function's values across all grid points within the variable's domain [40]. The Generalized Differential Quadrature Method (GDQM) often employs a Lagrange interpolated polynomial for the sake of comprehensiveness. The mathematical representation of this principle can be expressed by the equation:

$$\frac{d^m f(r)}{dr^m}@r = r_i = \sum_{i=1}^{N_r} C_{ij}^{(m)}(r)f(r_i) \tag{A.1}$$

Here, $C_{ij}^{(m)}(r)$ denotes the mth order derivative's weighting coefficients, which can be detailed through the GDQM method as:

$$C_{ij}^{(1)}(r) = \sum_{i=1}^{N_r} \frac{M^{(1)}(r_i)}{(r_j - r_i)M^{(1)}(r_j)} \text{ for } i,j = 1,2,3,\ldots,N_r \text{ and } i \neq j$$

$$C_{ii}^{(1)}(r) = -\sum_{j=1, j\neq i}^{N_r} C_{ij}^{(1)} \text{ for } i = 1,2,3,\ldots,N_r \tag{A.2}$$

The functions $M(r)$ and $M^{(1)}(r_{ii})$ are defined by:

$$M^{(1)}(r_{ii}) = \prod_{j=1}^{N_r}(r_i - r_j) \text{ for } i = 1,2,3,\ldots,N_r \tag{A.3}$$

Furthermore, higher order derivatives can be formulated using analogous methodology:

$$C_{ij}^{(2)}(r) = \sum_{k=1}^{N_r} C_{ik}^{(1)} C_{kj}^{(1)} \text{ for } i,j = 1,2,3,\ldots,N_r$$

$$C_{ij}^{(3)}(r) = \sum_{k=1}^{N_r} C_{ik}^{(1)} C_{kj}^{(2)} \text{ for } i,j = 1,2,3,\ldots,N_r \tag{A.4}$$

For the arrangement of grid points in radial and thickness directions, the study utilizes the nonuniform Chebyshev-Gauss-Lobatto approach as:

$$r_i = (r_o - r_i)\left(0.5 - 0.5\cos\left(\frac{(i-1)\pi}{N_r - 1}\right)\right) + r_i, \ i = 1,2,\ldots,N_r$$

$$z_i = -\frac{h}{2}\cos\left(\frac{(i-1)\pi}{N_z - 1}\right), \ i = 1,2,\ldots,N_z \tag{A.5}$$

References

[1] Cheung J.B., Chen T.S., Thirumalai K. Transient thermal stresses in a sphere by local heating 1974.

[2] Y. SUGANO, An analytical solution for a plane thermal stress problem in nonhomogeneous multiply connected regions: unaxisymmetric steady-state thermal stresses in a nonhomogeneous hollow circular plate, JSME Int. J. Ser 1, Solid Mech. Streng. Mater. 33 (1990) 136–144.

[3] M. Ishihara, Y. Tanigawa, R. Kawamura, N. Noda, Theoretical analysis of thermoelastoplastic deformation of a circular plate due to a partially distributed heat supply, J Therm Stress 20 (1997) 203–225.

[4] Y.O Tanigawa Yoshinobu, Three-dimensional transient thermal stresses of functionally graded rectangular plate due to partial heating, J. Therm. Stress. 22 (1999) 35–55.

[5] W.Z. Zhuang, N.S. Swansson, Localized thermal buckling due to hot streaks in a combustor liner, J. Propuls. Power 16 (2000) 661–665.

[6] T. Morimoto, Y. Tanigawa, R. Kawamura, Thermal buckling of functionally graded rectangular plates subjected to partial heating, Int. J. Mech. Sci. 48 (2006) 926–937.

[7] M. Ohmichi, N. Noda, Plane thermal stresses in a functionally graded plate subjected to a partial heating, J. Therm. Stress. 29 (2006) 1127–1142.

[8] Y. Ootao, Y. Tanigawa, Three-dimensional solution for transient thermal stresses of an orthotropic functionally graded rectangular plate, Compos. Struct. 80 (2007) 10–20, https://doi.org/10.1016/j.compstruct.2006.02.028.

[9] F. Fallah, A. Nosier, Nonlinear behavior of functionally graded circular plates with various boundary supports under asymmetric thermo-mechanical loading, Compos. Struct. 94 (2012) 2834–2850, https://doi.org/10.1016/j.compstruct.2012.03.029.

[10] K.R. Gaikwad, Analysis of thermoelastic deformation of a thin hollow circular disk due to partially distributed heat supply, J. Therm. Stress. 36 (2013) 207–224.

[11] M. Jabbari, S. Sohrabpour, M.R. Eslami, General solution for mechanical and thermal stresses in a functionally graded hollow cylinder due to nonaxisymmetric steady-state loads, J. Appl. Mech. 70 (2003) 111–118.

[12] M. Jabbari, A. Bahtui, M.R. Eslami, Axisymmetric mechanical and thermal stresses in thick short length FGM cylinders, Int. J. Press. Vessel Pip. 86 (2009) 296–306.

[13] M. Jabbari, E. Shahryari, H. Haghighat, M.R. Eslami, An analytical solution for steady state three dimensional thermoelasticity of functionally graded circular plates due to axisymmetric loads, Eur. J. Mech. - A/Solid. 47 (2014) 124–142, https://doi.org/10.1016/j.euromechsol.2014.02.017.

[14] Y. Ootao, M. Ishihara, Transient thermoelastic analysis for a multilayered hollow cylinder with piecewise power law nonhomogeneity due to asymmetric surface heating, Acta Mech. 225 (2014) 2903–2922.

[15] R. Kumar, L.S. Ramachandra, B. Banerjee, Nonlinear stability characteristics of composite cylindrical panel subjected to non-uniform in-plane mechanical and localized thermal loadings, Proc. India. Natl. Sci. Acad 82 (2016) 271–288.

[16] R. Kumar, L.S. Ramachandra, B. Banerjee, Semi-analytical approach for thermal buckling and postbuckling response of rectangular composite plates subjected to localized thermal heating, Acta Mech. 228 (2017) 1767–1791.

[17] V. Bhagat, J. P, Experimental investigation on buckling strength of cylindrical panel: effect of non-uniform temperature field, Int. J. Non Linear Mech. 99 (2018) 247–257, https://doi.org/10.1016/j.ijnonlinmec.2017.12.005.

[18] V.N. Van Do, T.H. Ong, C.-H Lee, Isogeometric analysis for nonlinear buckling of FGM plates under various types of thermal gradients, Thin-Walled Struct. 137 (2019) 448–462, https://doi.org/10.1016/j.tws.2019.01.024.

[19] D.A. Ehrhardt, L.N. Virgin, Experiments on the thermal post-buckling of panels, including localized heating, J. Sound Vib. 439 (2019) 300–309, https://doi.org/10.1016/j.jsv.2018.08.043.

[20] A. Amiri Delouei, A. Emamian, S. Karimnejad, H. Sajjadi, D Jing, Two-dimensional temperature distribution in FGM sectors with the power-law variation in radial and circumferential directions, J. Therm. Anal. Calorim. 144 (2021) 611–621.

[21] Y. Ren, R. Huo, D. Zhou, Thermo-mechanical buckling analysis of non-uniformly heated rectangular plates with temperature-dependent material properties, Thin-Walled Struct. 186 (2023) 110653, https://doi.org/10.1016/j.tws.2023.110653.

[22] A.E. Jeffers, Heat transfer element for modeling the thermal response of non-uniformly heated plates, Finite Elem. Anal. Des. 63 (2013) 62–68.

[23] L. Jiang, S. Chen, A. Usmani, Feasibility of dimensionally reduced heat transfer analysis for structural members subjected to localised fire, Adv. Struct. Eng. 21 (2018) 1708–1722.

[24] M.-X. Xiong, J.Y.R. Liew, Buckling behavior of circular steel tubes infilled with C170/185 ultra-high-strength concrete under fire, Eng. Struct. 212 (2020), 110523, https://doi.org/10.1016/j.engstruct.2020.110523.

[25] M.-X. Xiong, J.Y.R. Liew, Fire resistance of high-strength steel tubes infilled with ultra-high-strength concrete under compression, J. Constr. Steel Res. 176 (2021), 106410, https://doi.org/10.1016/j.jcsr.2020.106410.

[26] J.P. Petti, C. Lopez, R. Kalan, J.F. Dempsey, D. Villa, M.M. Hightower, et al., LNG Vessel Cascading Damage Structural and Thermal Analyses, Sandia National Lab. (SNL-NM),, Albuquerque, NM (United States); Sandia …, 2013.

[27] Kalan RJ, Petti JP. LNG cascading damage study volume I: Fracture testing Report. Sandia Natl Lab Rep NSAND2011-3342 2011.

[28] T. Baalisampang, F. Khan, R. Abbassi, V. Garaniya, Methodology to analyse LNG spill on steel structure in congested marine offshore facility, J. Loss Prev. Process Ind. 62 (2019), 103936.

[29] T. De Beer, B. Schrier, M Van Den Berg, Impact of cryogenic spills on FLNG hulls, in: CG Soares, J Parunov (Eds.), Trends Anal. Des. Mar. Struct. Proc. 7th Int. Conf. Mar. Struct, Dubrovnik, CRC Press, 2019, pp. 558–565.

[30] B.T. Oh, D.C. Lagoudas, S.C. Moon, Effect of insulation layer for thermal shock in cryogenic composite laminates, Polym. Compos. 34 (2013) 531–536.

[31] T. Iannaccone, G. Landucci, G.E. Scarponi, S. Bonvicini, V. Cozzani, Inherent safety assessment of alternative technologies for LNG ships bunkering, Ocean Eng. 185 (2019) 100–114.

[32] X. Li, W. Tang, Structural risk analysis model of damaged membrane LNG carriers after grounding based on Bayesian belief networks, Ocean Eng. 171 (2019) 332–344.

[33] M.S. Chun, M.H. Kim, W.S. Kim, S.H. Kim, J.M. Lee, Experimental investigation on the impact behavior of membrane-type LNG carrier insulation system, J. Loss Prev. Process Ind. 22 (2009) 901–907, https://doi.org/10.1016/j.jlp.2008.09.011.

[34] C.-S. Lee, J.-R. Cho, W.-S. Kim, B.-J. Noh, M.-H. Kim, J.-M. Lee, Evaluation of sloshing resistance performance for LNG carrier insulation system based on fluid-structure interaction analysis, Int. J. Nav. Archit. Ocean Eng. 5 (2013) 1–20, https://doi.org/10.2478/IJNAOE-2013-0114.

[35] Alireza Babaee, J. Jelovica, Nonlinear transient thermoelastic response of FGM plate under sudden cryogenic cooling, Ocean Eng. 226 (2021), 108875, https://doi.org/10.1016/j.oceaneng.2021.108875.

[36] J.N. Reddy, C.D. Chin, Thermomechanical analysis of functionally graded cylinders and plates, J. Therm. Stress 21 (1998) 593–626, https://doi.org/10.1080/01495739808956165.

[37] A. Babaee, J. Jelovica, Large amplitude vibration of annular and circular functionally graded composite plates under cooling thermal shocks, Thin-Walled Struct. 182 (2023), 110142.

[38] J.N. Reddy, Mechanics of Laminated Composite Plates and shells: Theory and Analysis, 2nd edition, CRC Press, Boca Raton, 2003, https://doi.org/10.1201/b12409.

[39] G.N. Praveen, J.N. Reddy, Nonlinear transient thermoelastic analysis of functionally graded ceramic-metal plates, Int. J. Solids Struct. 35 (1998) 4457–4476.

[40] C. Shu, Differential Quadrature and Its Application in Engineering, Springer, London, 2012, https://doi.org/10.1007/978-1-4471-0407-0.

[41] A. Babaee, M. Sadighi, A. Nikbakht, S. Alimirzaei, Generalized differential quadrature nonlinear buckling analysis of smart SMA/FG laminated beam resting on nonlinear elastic medium under thermal loading, J. Therm. Stress 41 (2018), https://doi.org/10.1080/01495739.2017.1408048.

[42] Z. Yang, D. Hurdoganoglu, S. Sahmani, B. Safaei, A. Liu, Surface stress size dependency in nonlinear thermomechanical in-plane stability characteristics of FG laminated curved nanobeams, Eng. Struct. 284 (2023), 115957, https://doi.org/10.1016/j.engstruct.2023.115957.

[43] R. Ansari, J. Torabi, R. Hassani, A comprehensive study on the free vibration of arbitrary shaped thick functionally graded CNT-reinforced composite plates, Eng. Struct. 181 (2019) 653–669.

[44] M.M. Keleshteri, J. Jelovica, Beam theory reformulation to implement various boundary conditions for generalized differential quadrature method, Eng. Struct. 252 (2022), 113666, https://doi.org/10.1016/j.engstruct.2021.113666.

[45] J.N. Reddy, An Introduction to Nonlinear Finite Element Analysis: With Applications to Heat transfer, Fluid mechanics, and Solid Mechanics, 2nd edition, Oxford University Press, 2014.